Copper hexacyanoferrate as a long-life cathode for aqueous aluminum ion batteries

Xiaoya Li[1], Angyin Wu[1], Caitian Gao[2], Zongkang Li[1], Seok Woo Lee[1,*]

[1] School of Electrical and Electronic Engineering, Nanyang Technological University, Singapore 639798, Singapore

[2] School of Physics and Electronics, Hunan University, Changsha 410082, P.R. China

[*] Corresponding author. Email: sw.lee@ntu.edu.sg

Abstract

Aqueous aluminum ion batteries (AAIBs) have emerged as promising low-cost and energy-dense alternatives to conventional lithium-ion batteries. However, AAIBs exhibit a poor rate capability and limited cycle life owing to the rapid degradation. In this study, a copper hexacyanoferrate (CuHCFe) electrode was introduced into AAIBs with an aluminum trifluoromethanesulfonate aqueous electrolyte. Common aluminum electrolytes were compared to highlight the effects of anions and pure acid solutions were examined to eliminate the concerns on proton. A reversible capacity of 69.35 mAh g^{-1} was obtained at 70 mA g^{-1}, with 73% capacity maintained at 50 C, exhibiting excellent rate performance. Furthermore, the types of anions played an important role in the electrochemical performance. With triflate anions, the CuHCFe electrode exhibited remarkable cycling stability with a neglectable capacity loss in 3000 cycles (eight months of continuous testing) at 70 mA g^{-1} and 70% retention after 2300 cycles at 350 mA g^{-1}. Ex situ characterization revealed that both transition metals in CuHCFe were simultaneously involved in the redox reaction with minimal lattice change upon ion insertion/extraction. The results demonstrate the compatibility and potential of CuHCFe

cathodes and aluminum triflate electrolytes for AAIBs, which can promote the development of such batteries for electrochemical energy storage.

Keywords: aqueous Al ion batteries, Prussian blue analogues, aluminum trifluoromethanesulfonate, energy storage, stability, rate performance

1 Introduction

Lithium-ion batteries represent a mature technology as the predominant rechargeable batteries for various energy storage devices. However, the limited availability of constituent materials, potential safety hazards, and high costs have driven the search for alternatives [1]. Low-cost, abundant alkaline and multivalent ions such as Na^+ [2], K^+ [3], Mg^{2+} [4], Zn^{2+} [5], and Al^{3+} [6] have emerged as promising candidates to manufacture rechargeable batteries. In particular, Al-ion batteries (AIBs) have attracted considerable attention owing to the abundance of Al in the Earth's crust, environmentally friendly construction of such batteries, and high volumetric capacity (8040 mAh cm^{-3}) and gravimetric capacity (2980 mAh g^{-1}) associated with the three-electron redox reaction.

Despite these advantages, research on AIBs is limited by the difficulty in identifying suitable electrolytes and cathode materials [7]. The widely used electrolytes that are considered to allow reversible stripping and plating of Al are ionic liquid electrolytes based on aluminum chloride and 1-ethyl-3-methylimidazolium chloride [8]. However, the ionic liquid electrolytes are typically expensive and moisture sensitive, causing safety risks and difficulties in commercialization [9]. The demand for electrochemically stable, low-cost, and environmentally friendly electrolytes has triggered the development of aqueous AIBs (AAIBs) [10]. In addition to common anion-based electrolytes such as $AlCl_3$, $Al(NO_3)_3$ and $Al_2(SO_4)_3$, a trifluoromethanesulfonate-based aqueous electrolyte, aluminum trifluoromethanesulfonate

($Al(OTF)_3$), has been proposed, which offers promising cycling stability owing to its high ionic conductivity, high oxidation voltage, and noncorrosive properties [11, 12].

Cathode materials typically exhibit low capacity and rapid cycling degradation [13]. Compared with monovalent ions, the ion mobility of multivalent ions in the host lattice is sluggish due to the strong columbic interaction that depends on the ionic radii and charge density of the guest ion. These ions are easily trapped in the host materials and lose their mobility. Al ions have a high charge density (three-electron configuration and ironic radius of 53.5 pm), which limits diffusion in the lattice, leading to slow kinetics. Graphite [14], metal oxides (VO_2 [15, 16], V_2O_5 [17, 18], TiO_2 [19–22], MnO_2 [23, 24], MoO_3 [25], etc.), phosphates [26], and Prussian blue analogues (PBAs) have been investigated as promising cathode materials [27–34]. PBAs are especially favorable for Al-ion insertion/extraction owing to their three-dimensional (3D) open framework, large interstitial sites, and low-cost synthesis. The chemical formula of PBAs is $A_xP[R(CN)_6]_y \cdot nH_2O$ (A is an alkali metal or alkaline earth metal such as Li, Na, K, Rb, or Cs; P is a nitrogen-coordinated transition metal such as Ag, Al, Cd, Co, Cr, Cu, Fe, Ga, In, Mn, Ni, or Pb; R is a carbon-coordinated transition metal such as Cr, Fe, Mn, or Co; and $0 \leq x \leq 2$, $y < 1$) [35]. If the ratio of P/R is 1, the PBA has a uniform channel size in the nanocubic framework. Otherwise, additional $R(CN)_6$ vacancies are present in the crystal. Both the channels and vacancies form interstitial spaces that promote the diffusion of guest ions [36]. Additionally, the interstitial water can shield the electrostatic field and facilitate ion transfer [37].

The use of PBAs for AAIBs was first examined by Liu et al. [27]. Copper hexacyanoferrate (CuHCFe) was used as an electrode in 0.5 M $Al_2(SO_4)_3$ aqueous electrolyte. An initial capacity of 41.0 mAh g^{-1} was achieved at a cycling rate of 10 C, which decayed to 54.9% of its initial value after 1000 cycles. Later, researchers examined the use of different dilute aqueous electrolytes such as pure $Al(NO_3)_3$ [28] and mixed $AlCl_3$ and KCl [29]. However, the capacity

of CuHCFe was lower than 50 mAh g^{-1}. Furthermore, similar electrode materials such as Prussian blue (FeHCFe) [30], nickel hexacyanoferrate (NiHCFe) [31], cobalt hexacyanoferrate (CoHCFe) [32], and manganese hexacyanoferrate (MnHCFe) were investigated [33, 34]. NiHCFe and CoHCFe exhibited low capacity of approximately 50 mAh g^{-1} and capacity retention of 47.3% (500 cycles at ~0.5 C) and 76% (1600 cycles at 2 C), respectively [31, 32]. Although FeHCFe and MnHCFe achieved a higher capacity (~110 mAh g^{-1}) [30, 33, 34], the capacity retention was low, typically less than 70% after 100 cycles, even in water-in-salt electrolytes. The maximum number of cycles observed in the studies was 100 at ~1 C [30], 5 C [33], or 25 C [34], implicitly indicating the low cycling stability of such materials.

Although the abovementioned studies highlighted the potential of PBAs as cathode materials for AAIBs, the obtained electrode exhibited low capacity and limited cycle life. Additionally, the storage mechanism of Al ions in various PBAs has not been comprehensively investigated. In this study, we considered the use of $Al(OTF)_3$ as aqueous electrolyte and examined the electrochemical performance of CuHCFe as a cathode material. Common electrolytes of aluminum nitrate ($Al(NO_3)_3$) and aluminum sulfate ($Al_2(SO_4)_3$) were also examined as comparison. Pure acid solutions were investigated to eliminate the effects of proton. Characterization analyses were performed to clarify the interaction between CuHCFe and Al ions during the redox reaction. The material exhibited remarkable rate performance with 73% capacity retained at a current rate of 50 C and a recovery efficiency of 96% to the initial C rate. Moreover, the material was stable during 3000 cycling tests (long cycle life), with a capacity retention of ~60 mAh g^{-1}. According to ex situ characterization, both the transition metals in CuHCFe were simultaneously involved in the reaction, with copper and iron being dominant at low and high potentials, respectively. The triflate anions enabled such high-rate and long-life electrochemical performance of CuHCFe. This research identifies a promising electrode material and electrolyte combination for the design of stable and durable AAIBs in energy storage applications.

2 Experimental Section

2.1 Material synthesis

CuHCFe nanoparticles were synthesized through a co-precipitation method. Equal amounts (60 mL) of 40 mM $Cu(NO_3)_2$ (Sigma-Aldrich, 61194) and 20 mM $K_3Fe(CN)_6$ (Alfa Aesar, 33357) were simultaneously dropwise added to deionized water (30 mL) by a peristaltic pump (0.5 mL min^{-1}) under magnetic stirring (300 rpm) at 40 °C. After 1 h stirring and 24 h precipitation, the yellowish green precipitate was filtered and sequentially washed with deionized water (three times) and acetonitrile (once). The powder was ground and collected after drying in a vacuum oven for 12 h at 40 °C.

2.2 Electrode preparation

A slurry of CuHCFe was prepared by grinding a mixture of 80 wt% CuHCFe powder, 15 wt% carbon black, and 5 wt% polyvinylidene fluoride (PVDF, Sigma-Aldrich, 182702), to which 1-methyl-2-pyrrolidinone (NMP, Sigma-Aldrich, 328634) was added as a solvent until a thick and smooth slurry was formed. The slurry was dropped onto carbon cloth (Fuel Cell Earth) with a mass loading of approximately 5 mg cm^{-2} and area of approximately 0.25 cm^2 and dried under vacuum for 12 h at 40 °C.

Activated carbon counter electrodes were prepared by grinding a mixture of 90 wt% activated carbon (Strem Chemicals, 06-0100) and 10 wt% PVDF and adding NMP to the powder until a thick and smooth slurry was formed. The slurry was dropped onto carbon cloth (Fuel Cell Earth) with high mass loading and dried under vacuum for 12 h at 40 °C.

2.3 Electrolyte preparation

The electrolytes were prepared by dissolving the corresponding salts in deionized water to attain the desired concentration. For example, deionized water was added to 0.5, 1, and 2 mM $Al(OTF)_3$ (Sigma-Aldrich, 515884) to make the total solution of 1 mL to get the concentrations of 0.5, 1, and 2 M, respectively. Similar method was applied to make 1 M $Al(NO_3)_3$ (Sigma-Aldrich, 237973) and 0.5 M $Al_2(SO_4)_3$ (Sigma-Aldrich, 368458) solutions. These solutions were used directly without adjusting pH. The nitric acid and trifluoromethanesulfonic acid solutions at a specific pH value were prepared by diluting the as-purchased nitric acid (Sigma-Aldrich, 438073) and trifluoromethanesulfonic acid (Sigma-Aldrich, 158534) with deionized water, respectively. The pH of each solution was measured by both the pH-indicator strips (MColorpHast^{TM}) and pH meter (ST300, Ohaus) at room temperature.

2.4 Electrochemical measurements

Electrochemical experiments were conducted in a three-electrode flooded beaker cell with a CuHCFe working electrode, an Ag/AgCl reference electrode, and an activated carbon counter electrode. Each electrode was fully oxidized to remove the residual potassium ions in the as-prepared CuHCFe framework and thoroughly washed with deionized water before any electrochemical test. All the tests were conducted with a calibrated Ag/AgCl pseudo-reference electrode (Fig. S1), except for the long-term test at 70 mA g^{-1}, in which a standard Ag/AgCl reference electrode was used. A potentiostat (VMP3, Biologic) was used to obtain the electrochemical measurements.

2.5 Material characterization

Scanning electron microscopy (SEM) and energy-dispersive X-ray spectroscopy (EDS) analyses were performed using a JEOL FESEM 7600F device. Ultra-high resolution (UHR) transmission electron microscopy (TEM) was performed using a JEOL 2010 UHR device. X-ray diffraction (XRD) patterns were collected using a Bruker D8 Advance Powder instrument

with a Cu–Kα radiation source (λ = 1.5406 Å). The lattice parameters were calculated through Rietveld refinements. Thermogravimetric analysis (TGA) was conducted from 25 °C to 600 °C using Shimadzu DTG60 with N_2 purging. X-ray photoelectron spectroscopy (XPS) analyses were performed using a Kratos AXIS Supra with an Al–Kα excitation source. To prepare the electrodes for characterization, firstly, the CuHCFe electrode was charged to the upper cut-off voltage to remove the residual potassium ions in the as-prepared electrode. Then the electrode was thoroughly washed with deionized water and transferred to a new three-electrode system with fresh electrolyte. After one cycle charging and discharging, unless otherwise stated, it was reduced or oxidized to the desired state of charge at 70 mA g^{-1}. The electrodes were thoroughly washed with deionized water and dried under vacuum for 12 h at 40 °C before characterization.

3 Results and Discussion

3.1 Morphology and structure of CuHCFe

According to the SEM and TEM images, the as-synthesized CuHCFe powder was composed of uniformly distributed nanoparticles with smooth surfaces sized approximately 100 nm (Fig. 1a). In the XRD spectrum, the main characteristic diffraction peaks of CuHCFe can be observed at 2θ of 15.15°, 17.53°, 24.84°, 35.42°, 39.76°, 43.75°, 50.95°, 54.27°, and 57.49°, corresponding to a face-centered cubic structure (space group of *Fm-3m*, ICSD code: 252537). All the main peaks are strong and sharp, indicating the high crystallinity of CuHCFe (Fig. 1b). The lattice parameter is $a = b = c$ = 10.166 Å, calculated using the Rietveld refinement method. According to the TGA (Fig. S2), the powder experienced significant weight losses at temperatures less than 100 °C and 200 °C (18.5 wt% and 19.5 wt%, respectively), attributable to the loss of the surface absorbed water and interstitial water, respectively. The synthesized CuHCFe is an imperfect PBA with defects, and its molecular formula is $K_{0.03}Cu[Fe(CN)_6]_{0.65}\cdot nH_2O$, with n calculated to be 2.7. This observation is consistent with

reported findings on the same material [36] and suggests that the pristine material is almost fully oxidized. According to the chemical formula, the maximum capacity is 69.3 or 106.5 mAh g^{-1} if solely Fe or Cu are reduced, respectively. However, the specific capacity may be less than the theoretical values owing to the presence of zeolitic water that can occupy the available sites for guest ion insertion. Hence, in this paper, all C rates cited are based on a capacity of 70 mAh g^{-1} (e.g., 1 C = 70 mA g^{-1}). The crystal structure of CuHCFe is schematically illustrated in Fig. 1c. C and N ends of the bridged cyanide ligands are coordinated with the Fe and Cu atoms in octahedral configurations, creating a porous 3D cubic framework ideally enclosing interstitial cages containing the trapped zeolitic water molecules [38, 39]. These cages are termed A sites; they have a diameter of 4.6 Å and form open <100> channels with a diameter of 3.2 Å [36], allowing the diffusion of various guest ions (diffusion path I, illustrated by a hydrated K ion). Notably, the imperfect CuHCFe has ferro- and ferri-cyanide vacancies. The exposed Cu ions are "passivated" by the ligand water molecules in the vacancies [38, 39]. These ligand water molecules can shield the charge from the insertion ions and weaken the interaction with the host materials, thereby facilitating the ion transport. If these vacancies appear on adjacent sites and connect with each other, they will create an alternative pathway with enlarged open channels for guest ion intercalation (diffusion path II, illustrated by a hydrated Al ion). The insertion of monovalent ions such as Na^+, K^+, and Rb^+ into PBA materials has been extensively investigated [40, 41], and it is widely accepted that these ions are mostly inserted into the central A sites after partial dehydration [42]. In comparison with monovalent ions, multivalent ions have higher charge densities and form larger hydration shells owing to the stronger electrostatic interactions with the dipoles of water molecules. Although the bare ionic radius of Al^{3+} is small (0.53 Å), hydrated Al^{3+} has a large effective radius (4.75 Å) [4]. The large hydrated Al^{3+} ion is expected to be thermodynamically stable and reside in the vacancy sites owing to the shielding effect of the hydration shell, similar to that of Mg^{2+}, Pb^{2+}, and Y^{3+} [36, 43]. Hence, multiple possible diffusion pathways emerge upon the insertion of Al^{3+} into CuHCFe: through the <100>

channels along the x-axis with a one-step dehydration process, through the connected vacancies corresponding to several-step dehydration processes, or both. Both mechanisms and their combination may contribute to the ion diffusion in the CuHCFe framework, resulting in multiple insertion voltages owing to the different degrees of free energy changes related to the dehydration during insertion.

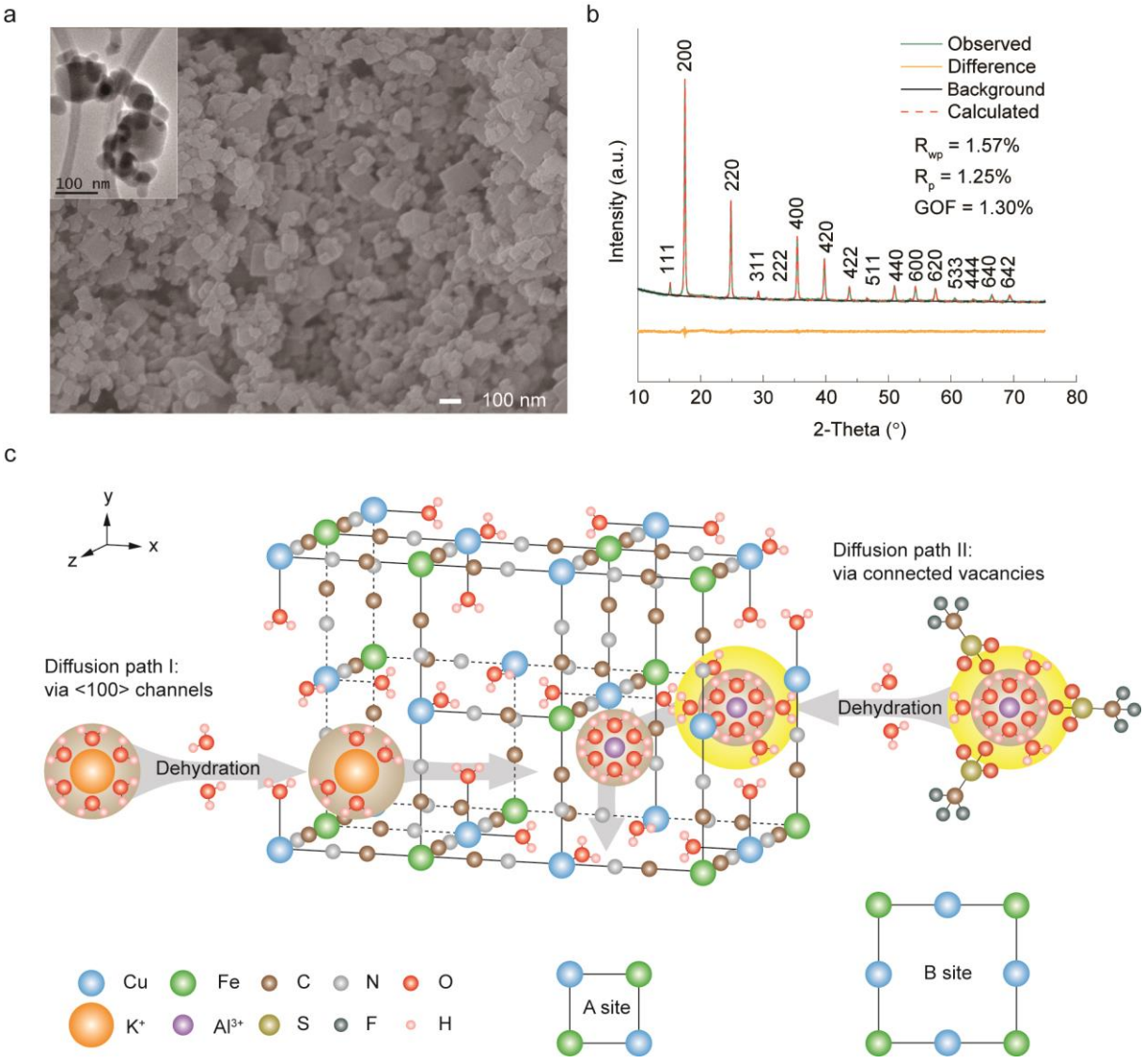

Fig. 1. Characterization of CuHCFe powder. (a) SEM image. The inset was the TEM image. (b) XRD spectrum and the Rietveld refinement results. (c) Corresponding crystal structure with two possible diffusion paths. Diffusion path I was through <100> channels. Diffusion path II was through enlarged open channels by the connected ferro- and ferri-cyanide vacancies.

3.2 Electrochemical performance of CuHCFe

The electrochemical properties of CuHCFe were investigated in a three-electrode system. Fig. 2a shows the cyclic voltammetry (CV) curve of CuHCFe in 1 M $Al(OTF)_3$ electrolyte at a scan rate of 1 mV s^{-1}. Broad redox peaks can be observed over a wide potential window between 0.16 and 1.36 V vs. the standard hydrogen electrode (SHE). Two main redox peaks centered at 0.65/0.50 V and 1.13/1.02 V (vs. SHE) for O1/R1 and O2/R2 can be observed, indicating that Al^{3+} participates in a two-step reaction with CuHCFe. In accordance, two slanted charging and discharging plateaus can be observed in the galvanostatic cycling with potential limitation (GCPL) curve (Fig. 2b), delivering a specific capacity of 69.35 mAh g^{-1} and coulombic efficiency of 98.90% at a current density of 70 mA g^{-1}. The flipped discharging curve (in red) is suggestive of non-symmetric insertion and extraction processes. It is hypothesized that the large hydration sheaths of Al^{3+} and the interstitial water molecules in the CuHCFe framework coordinately shield the charged ions upon insertion, resulting in the fast kinetics and high mobility of Al^{3+} ions. However, the partially dehydrated Al^{3+} ions exhibit slow diffusion upon extraction owing to the strong electrostatic field. Consequently, the two charging plateaus are not clearly separated, unlike those in the discharging curve. In particular, the charging process at a high potential is sluggish with large hysteresis, as demonstrated by the galvanostatic intermittent titration (GITT) curve presented in Fig. 2c and Fig. S3. The electrochemical performance of CuHCFe in various $Al(OTF)_3$ electrolyte concentrations of 0.01, 0.02, 0.05, 0.1, 0.2, 0.5, and 2 M was also examined and presented in Fig. S4.

The electro-kinetic characteristics were analyzed to clarify the Al ion storage mechanism. Fig. 2d shows the CV curves obtained at scan rates (v) ranging from 0.1 to 5 mV s^{-1}. With the increase in the scan rate, the oxidation and reduction peaks shift to higher and lower potentials, respectively, owing to the enhanced polarization. The relationship between the redox peak current density and scan rate is shown in Fig. 2e. The peak current densities of O1, O2, R1, and

R2 vary linearly with the square root of the scan rate ($v^{1/2}$), suggestive of diffusion-controlled faradaic processes (Table S1). The rate performance was examined by GCPL in the potential window of 0.16–1.36 V vs. SHE at various current densities ranging from 35 mA g^{-1} (0.5 C) to 3.5 A g^{-1} (50 C). The variations in the capacity and coulombic efficiency with respect to the cycle number are presented in Fig. 2f and Table S2. The typical GCPL curves at each C rate are presented in Fig. 2g. The CuHCFe electrode exhibits an average specific capacity of 64.94 mAh g^{-1} and average coulombic efficiency of 97.43% at 0.5 C. The specific capacity decreases and coulombic efficiency increases with increasing the current density. The specific capacity at 50 C is 47.50 mAh g^{-1}, which is 73% of that at 0.5 C. The capacity loss is attributable to the shrinkage of the high potential plateau (O2/R2) owing to the potential drop associated with the large hysteresis (~40 mV, Fig. 2c) when charging process shifts to discharging process (Fig. 2g). The average coulombic efficiency at 50 C is 99.92%. The discharge capacity can be recovered to 62.55 mAh g^{-1} when the C rate returns to 0.5 C. These results suggest that the CuHCFe electrode in 1 M $Al(OTF)_3$ aqueous electrolyte exhibits a high rate capability and coulombic efficiency even at 50 C.

The long-term stability of CuHCFe in 1 M $Al(OTF)_3$ aqueous electrolyte was tested at two current densities. At 70 mA g^{-1}, as given in Fig. 2h, the discharge capacity exhibits negligible degradation with an average value of 61.48 mAh g^{-1} across 3000 cycles. The coulombic efficiency increases from 95.35% to 99.58% in the first 100 cycles and is then maintained throughout the tests. At a high current density of 350 mA g^{-1}, as shown in Fig. 2i, the discharge capacity remains nearly constant at approximately 60 mAh g^{-1} without any apparent loss within 500 cycles. Subsequently, this capacity gradually decays, but its value is 70% of the initial capacity even after 2300 cycles. The corresponding GCPL curves for the 1st, 10th, 100th, 100th, and 2300th cycles are shown in Fig. 2j. The high-potential plateau is enlarged, and the low-potential plateau shrinks. The phenomenon was further examined by ex situ XRD, XPS, and EDS and discussed in Section 3.4.

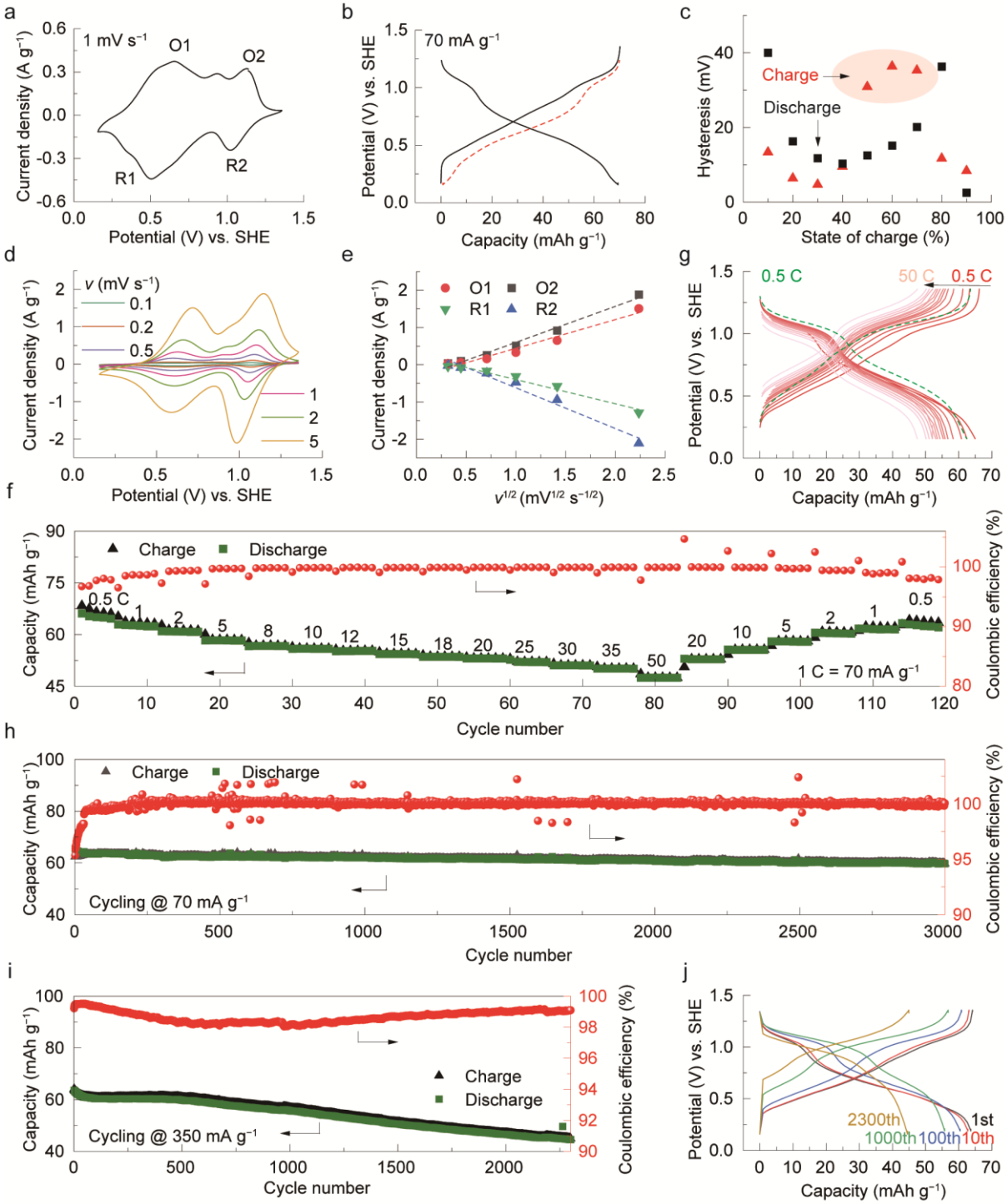

Fig. 2. Electrochemical performance of CuHCFe in 1 M $Al(OTF)_3$ aqueous electrolyte. (a) CV curve at a scan rate of 1 mV s^{-1}. (b) GCPL curve at a current density of 70 mA g^{-1}. The red dash line was the flipped discharge curve. (c) Hysteresis of the potential profile in terms of state of charge by the GITT technique at 70 mA g^{-1}. (d) CV curves at various scan rates (v). (e)

Linear fit of the peak current density vs. the square root of the scan rate ($v^{1/2}$). (f) Rate performance from 0.5 C to 50 C. (g) Typical GCPL curves at each C rate from 0.5 C to 50 C (solid lines) and the recovered GCPL at 0.5 C (dash line). (h) Long-term stability at 70 mA g^{-1}. (i) Long-term stability at 350 mA g^{-1}. (j) GCPL curves at 350 mA g^{-1} for the 1st, 10th, 100th, 1000th, and 2300th cycles.

3.3 Mechanism of Al ion storage in CuHCFe

To identify the reaction chemistry, ex situ characterization by XRD and XPS was performed. Fig. 3a shows the XRD patterns of eight CuHCFe electrodes at various potentials (left panel), including full spectra (middle panel) and magnified spectra of (4 0 0) peaks (right panel). The main characteristic diffraction peaks are maintained in the full spectra, similar to that for the CuHCFe powder, and can be indexed to the face-centered cubic *Fm-3m* space group. However, the position of the main peaks is slightly different, corresponding to lattice shrinkage upon ion insertion into the crystalline structure and reversible lattice expansion upon ion extraction. The lattice parameters were derived from the XRD full patterns by Rietveld refinement (Fig. S5 and Table S3). As shown in Fig. 3b, the initial lattice parameter is 10.050 Å in the fully reduced state (state 1), it linearly increases to 10.120 Å in the fully oxidized state (state 4), and it decreases to 10.037 Å when CuHCFe is fully reduced again (state 8). These findings demonstrate that CuHCFe undergoes a reversible redox reaction with Al^{3+} (de)intercalation. Moreover, the lattice shrinkage from 10.120 Å to 10.037 Å corresponds to a small volume change of 2.5%. The minimal volume variation may be responsible for the remarkable cycling stability of CuHCFe with Al ion insertion/extraction.

The oxidation states of transition metal ions in CuHCFe were investigated to clarify the redox evolution during the Al^{3+} (de)intercalation. The Fe 2*p*, Cu 2*p*, and Al 2*p* spectra for CuHCFe electrodes at different cut-off potentials are presented in Figs. 3c–e, respectively. The Fe 2*p* spectra can be decomposed into several components with Fe^{2+}, Fe^{3+}, and their satellites.

Specifically, the components in the Fe 2$p_{3/2}$ spectra are Fe^{2+}, Fe^{3+}, Fe^{2+} satellite, and Fe^{3+} satellite at binding energies of 709.3, 710.8, 715.9, and 721.1 eV, respectively. The Cu 2*p* (Cu 2$p_{3/2}$) spectra can be decomposed into the following components: Cu^{+}, Cu^{2+}, and Cu^{2+} satellites at binding energies of 933.8, 936.5, and 945.0 eV, respectively. Because the photoelectron line positions of Al 2*p* and Cu 3*p* nearly overlap, the main components in the Al 2*p* (Al 2$p_{3/2}$) spectra are Cu^{+} 3*p*, Cu^{2+} 3*p*, and Al^{3+} 2*p*, corresponding to binding energies of 76.7, 78.7, and 75.7 eV, respectively. In the charging process (states 1–4), Fe^{2+} and Cu^{+} are oxidized to Fe^{3+} and Cu^{2+}, respectively, and Al^{3+} ions are extracted, as indicated by the decreased intensity. In the following discharging process (states 5–8), Fe^{3+} and Cu^{2+} are reduced to Fe^{2+} and Cu^{+}, respectively, and Al^{3+} ions are inserted, indicated by the intensified Al^{3+} 2*p* peaks. Moreover, the intercalation of Al^{3+} is further demonstrated by the EDS elemental mappings (Fig. S6). The elemental contents in each valence state were obtained from the XPS fitting results for the atomic ratios of Al to Fe (Fig. 3f), Fe^{2+} to Fe^{3+} (Fig. 3g), and Cu^{+} to Cu^{2+} (Fig. 3h). The proportions of both Fe^{2+} and Cu^{+} decrease with the decrease in the atomic ratio of Al/Fe, and vice versa, indicating that both Fe and Cu are simultaneously involved in the reaction. At fully discharged state, the atomic ratio of Al to Fe is about 0.37. The variation in Cu^{+}/Cu^{2+} is more significant at low potentials (states 1–2 and 6–8) than at high potentials (states 3–4 and 4–5), and the valence state of Fe exhibits the opposite trend. This finding indicates that Cu and Fe are dominant in the reaction at low potentials (O1/R1, Fig. 2a) and high potentials (O2/R2, Fig. 2a), respectively. The ligand field stabilization energy of low-spin Fe has been noted to be higher than that of high-spin Cu, resulting in an enhanced redox potential of Fe^{2+}/Fe^{3+} [31]. The atomic ratio of Al to Fe was also examined by EDS (Fig. S7 and Table S4). The results are matched well with the XPS fitting results. As confirmed by XPS and EDS characterizations, the reversible insertion/extraction mechanisms of Al ion can be expressed as:

$$Cu[Fe(CN)_6]_{0.65} + 0.24\,Al^{3+} + 0.72e^{-} \leftrightarrow Al_{0.24}Cu^{I}_{0.69}Cu^{II}_{0.31}[Fe^{II}(CN)_6]_{0.30}[Fe^{III}(CN)_6]_{0.35} \quad (1)$$

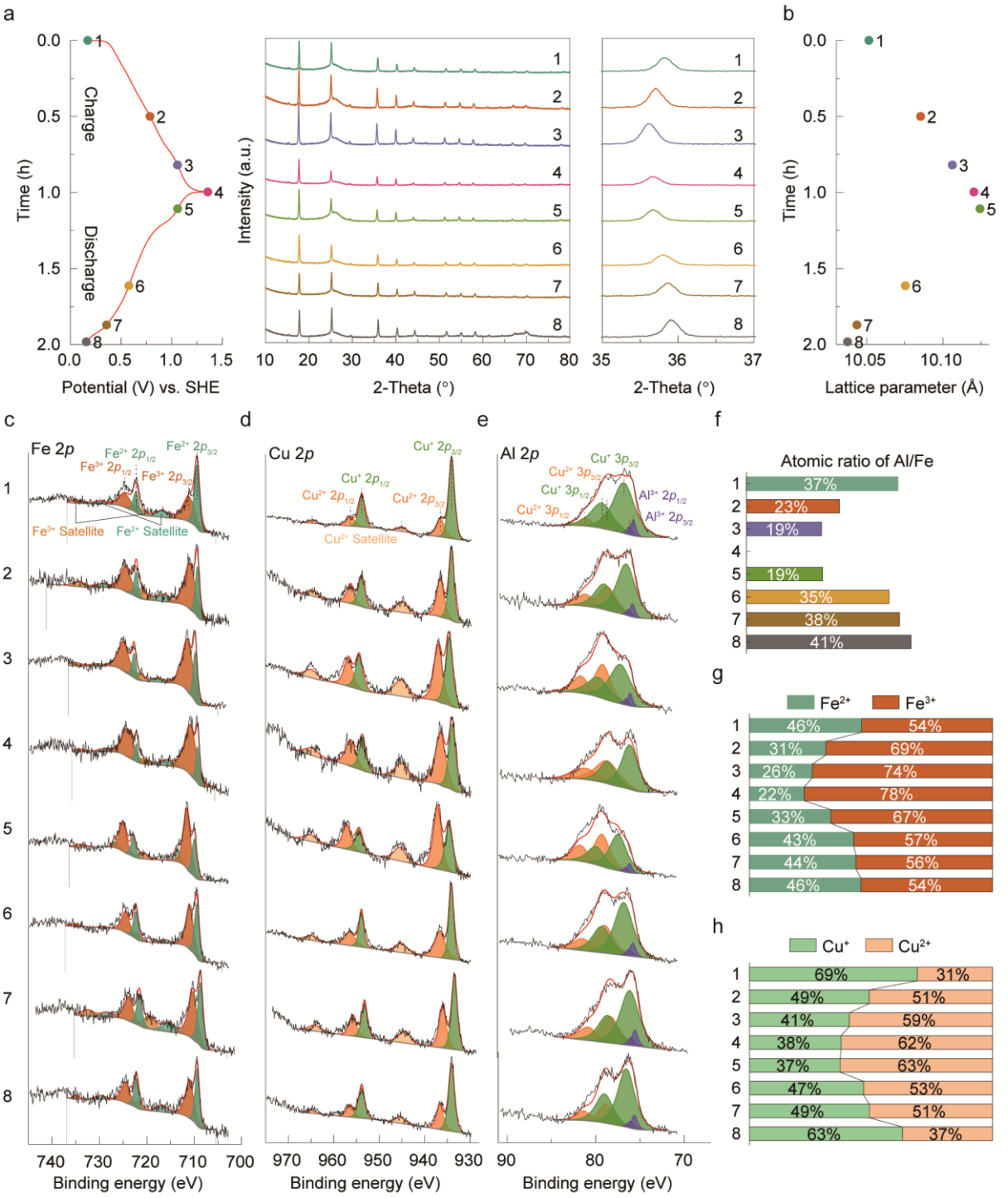

Fig. 3. Ex situ characterization of CuHCFe with Al ion insertion/extraction. (a) XRD patterns for eight electrodes at various potentials (left panel), including the full spectra (middle panel) and magnified spectra of (4 0 0) peaks (right panel). (b) Lattice parameter variations derived by the Rietveld refinement. (c–e) XPS patterns of Fe 2*p* (c), Cu 2*p* (d), and Al 2*p* (e) for the eight

electrodes. (f–h) XPS fitting results for the atomic ratios of Al to Fe (f), Fe^{2+} to Fe^{3+} (g), and Cu^{+} to Cu^{2+} (h).

3.4 Discussion and comparison with literatures

We firstly discussed on the capacity contribution variation during cycling. We noticed that the GCPL curve is changing with the high-potential plateaus enlarging with cycling (Fig. 2j). According to the above XPS analysis, Fe contributes to an increasing portion of the capacity with cycling. To further examine this phenomenon, electrode samples were prepared at various states of charge after 90 cycles of charging and discharging at 70 mA g^{-1} and characterized by XPS, XRD, and EDS (Figs. S8 and S9). As shown in Fig. S8a, the redox peak at a high potential (O2/R2) is narrower and more intensified, indicating that the redox reaction at O2/R2 is more kinetically favored. Fig. S8b shows the corresponding GCPL curve. A discharge capacity of 61.01 mAh g^{-1} is achieved at 70 mA g^{-1}, with high- and low-potential plateaus contributing nearly equally to the capacity. The valence states of Fe, Cu, and Al for the five CuHCFe electrodes at different potentials (Fig. S8c) are shown in Figs. S8d–f, respectively. The extracted quantification results for the atomic ratios of Al to Fe, Fe^{2+} to Fe^{3+}, and Cu^{+} to Cu^{2+} are shown in Figs. S8g–i, respectively. In the high-potential reaction, the proportion of Fe^{2+} first decreases from 47% (state 2) to 22% (state 3, fully oxidized) and then increases to 32% (state 4). In contrast, the percentage of Cu varies from 33% (state 2) to 15% (state 3) to 18% (state 4). The greater variation in the valence states of Fe than those of Cu proves the hypothesis that the redox reaction of Fe makes a larger contribution to the capacity at high potentials. The cubic framework of CuHCFe is maintained, the insertion of Al^{3+} is observed (Fig. S8j and Fig. S9).

Then, we discussed on the effects of anions. Common solutions of 1 M $Al(NO_3)_3$ and 0.5 M $Al_2(SO_4)_3$ without adjusting pH were adopted as the electrolytes; the electrochemical performance results of CuHCFe (CV, GCPL, rate performance, and long-term stability) are

shown in Fig. S10 and Fig. S11, respectively. The shapes of the CV and GCPL curves are similar to those in the case of $Al(OTF)_3$. Slight variations are observed on the peak positions and relative current density ratios at each redox peak (Fig. S10b and Fig. S11b). At 70 mA g^{-1}, CuHCFe delivers a specific capacity of 63.33 and 60.79 mAh g^{-1} in $Al(NO_3)_3$ and $Al_2(SO_4)_3$ electrolytes, which is 8.7% and 12.3% less than that in $Al(OTF)_3$, respectively (Fig. S10c and Fig. S11c). The rate performance results at current densities from 35 mA g^{-1} (0.5 C) to 3.5 A g^{-1} (50 C) demonstrate the feasibility of Al^{3+} insertion/extraction in CuHCFe across a wide range of current rates in the presence of NO_3^- and SO_4^{2-} anions (Fig. S10d–e, Fig. S11d–e). However, the capacity retention at 50 C with SO_4^{2-} is only 54% of that at 0.5 C, much lower than that with NO_3^- and OTF^- (~73%), indicating poor rate capability caused by SO_4^{2-} (Table S2). The long-term stability tests show that CuHCFe can only survive 680 and 290 cycles with NO_3^- and SO_4^{2-}, respectively, until the capacity decays to 70% of the initial capacity (Fig. S10f–g, Fig. S11f–g), much shorter than 2300 cycles with OTF^-. Hence, for Al^{3+} storage in CuHCFe, the anion preference is $OTF^- > NO_3^- > SO_4^{2-}$. The insertion/extraction mechanism is Al-ion diffusion-controlled faradaic processes (Fig. S2d–e, Fig. S12, Table S1, Table S5, and Table S6). The diffusion coefficient (D, $cm^2\ s^{-1}$) of Al^{3+} ion can be estimated by Randles-Sevick equation [44]:

$$i = 0.4463(F^3/RT)^{1/2} n^{3/2} A D^{1/2} C v^{1/2} \quad (2)$$

where i is the peak current, A; F is Faraday constant, C mol^{-1}; R is the universal gas constant, J $mol^{-1}\ K^{-1}$; T is the temperature, K; n is the number of electrons; A is the surface area of electrode, cm^2; C is the concentration of Al ions in the electrolyte, mol cm^{-3}; v is the scan rate, V s^{-1}. The Al ion diffusion coefficients in the presence of OTF^- are calculated to be 1.99×10^{-8}, 3.59×10^{-8}, 1.62×10^{-8}, and 3.20×10^{-8} $cm^2\ s^{-1}$ for redox peak O1, O2, R1, and R2, respectively. They are one order of magnitude larger than those in the presence of NO_3^- and SO_4^{2-} (Table S7), indicating better kinetics enabled by OTF^-. Additional molecular dynamic simulations must be performed to clarify the role of the anions and corresponding mechanism.

Thirdly, we examined the effects of pH and proton. As given in Fig. 4a and Table S8, the pH values of the as-prepared 1 M $Al(OTF)_3$, 1 M $Al(NO_3)_3$, and 0.5 M $Al_2(SO_4)_3$ are 2.29, 1.60, and 2.58, respectively. Although $Al(NO_3)_3$ electrolyte is more acidic, it contrarily causes worse long-term stability than $Al(OTF)_3$. Likewise, $Al_2(SO_4)_3$ results in the worst long-term stability although it has similar pH with the other two solutions. Since anion is the only variable in the examined cases, it is reasonable to infer that anion, rather than proton, makes the differences in the electrochemical performance of Al^{3+} storage in CuHCFe. To further confirm this, we prepared the pure nitric acid (HNO_3) and trifluoromethanesulfonic acid (HOTF) solutions at a similar pH with 1 M $Al(OTF)_3$ and investigated the electrochemical performance of CuHCFe (Fig. S13). As shown in Fig. S13b and Fig. 13d, broader redox peaks are observed in HOTF, while there are four pairs of redox peaks in HNO_3. This contrasts with the two-redox-pair behavior of topochemistry of Al^{3+} in CuHCFe. The results indicate that proton (de)insertion is quite distinct from Al ion storage in CuHCFe. The proton transfer is reported to be a diffusion-free Grotthuss conduction with a contiguous hydrogen-bonding network [45]. The long-term tests show CuHCFe has short cycle lives, i.e., 48 cycles and 30 cycles, in HOTF and HNO_3, respectively, till 70% capacity retention (Fig. S13f–i and Fig. 4b). The distinction between the (de)protonation behaviors in these two acids also reveal that anion matters in redox reactions, which warrants further investigation.

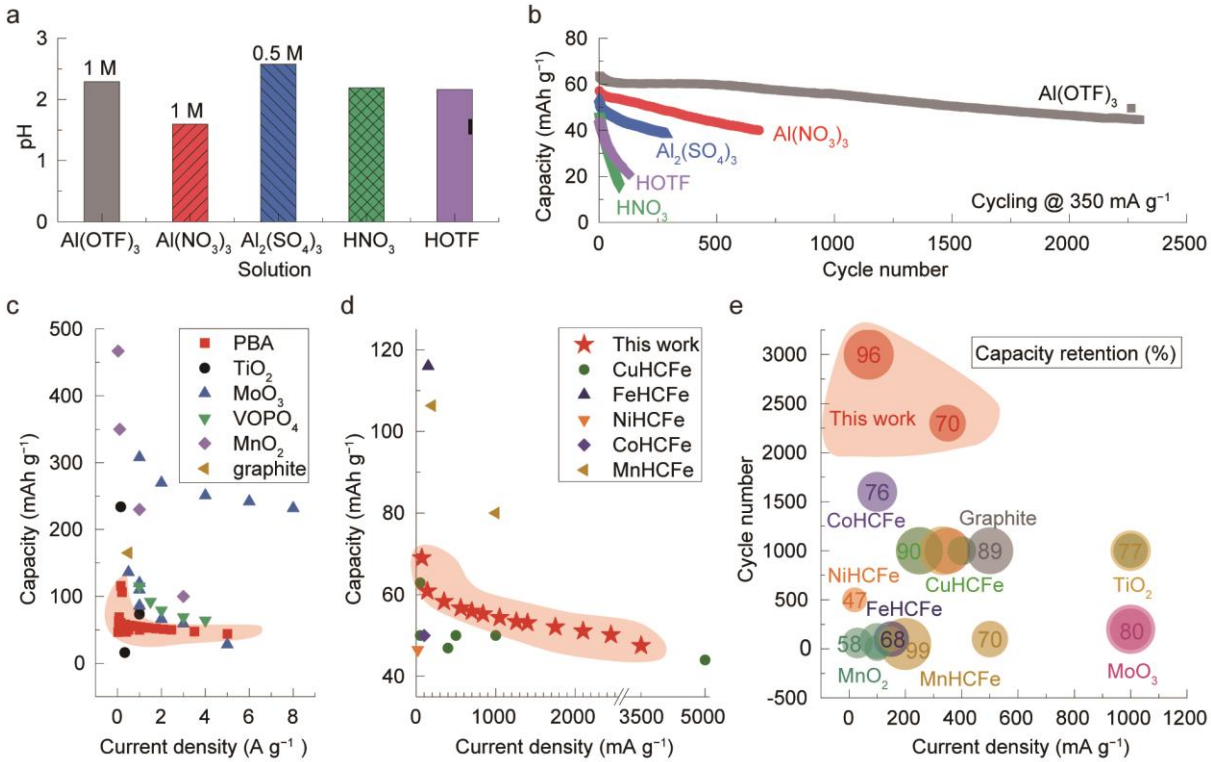

Fig. 4. Comparison with other electrolytes and literatures. (a) pH value of the examined solutions. (b) Comparison of long-term stability of CuHCFe in the examined solutions. (c) Comparison of specific capacity vs. current density for the studied materials in AAIBs. (d) Comparison of specific capacity vs. current density for PBA materials in AAIBs. (e) Comparison of capacity retentions with respect to current density and cycle numbers for the studied materials in AAIBs. The bubble size represents the capacity retention ratio to the initial capacity. Numerical values are summarized in detail in Table S9.

Finally, we compared the performance of the proposed framework with that of existing AAIBs. Detailed results are summarized in Table S9. Fig. 4c shows a comparison of the capacity in terms of the current densities corresponding to materials that have been considered for use in AAIBs: PBAs [27–34], TiO_2 [19–22], MoO_3 [25], $VOPO_4$ [26], MnO_2 [23, 24], and graphite [14]. Metal oxides outperform other materials in terms of the specific capacity. MnO_2 exhibits the highest capacity of 467 mAh g^{-1} at a current density of 30 mA g^{-1} when tested in the water-in-salt $Al(OTF)_3$ electrolyte [23]. However, this capacity decreases to 350 mAh g^{-1}

at 100 mA g^{-1} or 230 mAh g^{-1} at 1000 mA g^{-1} if a dilute electrolyte is used [12]. In comparison, the capacity of PBAs is lower (typically less than 60 mAh g^{-1}). Fig. 4d shows a detailed comparison of the PBA materials reported so far. It clearly shows that our work exhibits the highest performance in terms of the specific capacity and rate performance across a wide current density range. Fig. 4e shows a comparison of the cycle life and long-term stability of all the studied materials. Metal oxides exhibit a low capacity retention. For example, the capacity is less than 70% of the initial value for MnO_2 within 80 cycles at low current density, 80% for TiO_2 within 1000 cycles at ~15 C in the water-in-salt electrolyte, and 80% for MoO_3 within 200 cycles at ~10 C. PBAs exhibit a longer cycle life than other materials, with the proposed framework achieving the highest long-term stability. At 350 mA g^{-1}, CuHCFe can survive 2300 cycles in the $Al(OTF)_3$ electrolyte until the capacity decays to 70% of its initial value. Furthermore, at 70 mA g^{-1}, the discharge capacity exhibits negligible degradation, and the capacity retention is 96% even after 3000 cycles (eight months of continuous testing). Overall, metal oxides exhibit high specific capacity but low stability. PBAs exhibit a reasonable specific capacity and stability. The proposed combination of the electrode material and electrolyte can promote the development of AAIBs with long cycle lives.

4. Conclusion

CuHCFe exhibited excellent electrochemical performance as a cathode for AAIBs with an aluminum trifluoromethanesulfonate aqueous electrolyte. A reversible discharge capacity of 69.35 mAh g^{-1} was obtained at a current density of 70 mA g^{-1} with both Fe^{2+}/Fe^{3+} and Cu^{+}/Cu^{2+} redox pairs activated and involved in the reaction. At high and low potentials, Fe^{2+}/Fe^{3+} and Cu^{+}/Cu^{2+} contributed more to the capacity, respectively. The comparison results with the common aqueous electrolytes indicated that for Al^{3+} storage in CuHCFe, the anion preference was $OTF^{-} > NO_3^{-} > SO_4^{2-}$. In the presence of triflate anions, CuHCFe exhibited excellent rate

capability, as the capacity was 73% when the C rate was significantly increased by 100 times, and the recovery efficiency was 96% when the C rate returned to the initial value. Furthermore, CuHCFe exhibited excellent cycling stability with 96% capacity retention even after eight months of continuous testing (3000 cycles), with the crystal structure well-maintained (crystal volume change of 2.5% upon ion insertion/extraction). The proposed electrode material and electrolyte combination can promote the development of future aqueous AAIBs with long lifetimes.

CRediT author statement

X. Li: Conceptualization, Methodology, Validation, Formal analysis, Investigation, Data Curation, Writing - Original Draft, Writing - Review & Editing, Visualization; **A. Wu:** Formal analysis; **C. Gao:** Resources; **Z. Li:** Investigation; **S.W. Lee:** Writing - Original Draft, Writing - Review & Editing, Supervision, Funding acquisition.

Data availability

The data that support the findings of this study are available from the corresponding author upon reasonable request.

Declaration of Competing Interests

The authors declare no conflict of interest. The authors declare that they have no known competing financial interests or personal relationships that could have appeared to influence the work reported in this paper.

Acknowledgements

S.W.L. acknowledges the support by the National Research Foundation, Prime Minister's Office, Singapore under its NRF-ANR Joint Programme (NRF2019-NRF-ANR052 KineHarvest). The authors would like to acknowledge the Facility for Analysis, Characterization, Testing and Simulation (FACTS), Nanyang Technological University, Singapore, for use of their SEM, XRD, TEM, and XPS facilities.

Appendix A. Supporting Information

Supporting Information is available online.

References

[1] F. Duffner, N. Kronemeyer, J. Tübke, J. Leker, M. Winter, R. Schmuch, Post-lithium-ion battery cell production and its compatibility with lithium-ion cell production infrastructure, Nat. Energy 6 (2021) 123–134. https://doi.org/10.1038/s41560-020-00748-8.

[2] K. Chayambuka, G. Mulder, D.L. Danilov, P.H.L. Notten, Sodium-ion battery materials and electrochemical properties reviewed, Adv. Energy Mater. 8 (2018) 1800079. https://doi.org/10.1002/aenm.201800079.

[3] X. Min, J. Xiao, M. Fang, W. Wang, Y. Zhao, Y. Liu, A.M. Abdelkader, K. Xi, R. Vasant Kumar, Z. Huang, Potassium-ion batteries: outlook on present and future technologies, Energy Environ. Sci. 14 (2021) 2186. https://doi.org/10.1039/D0EE02917C.

[4] Y. Liu, G. He, H. Jiang, I.P. Parkin, P.R. Shearing, D.J.L. Brett, Cathode design for aqueous rechargeable multivalent ion batteries: challenges and opportunities, Adv. Funct. Mater. 31 (2021) 2010445. https://doi.org/10.1002/adfm.202010445.

[5] Q. Ni, B. Kim, C. Wu, K. Kang, Non-electrode components for rechargeable aqueous zinc batteries: electrolytes, solid-electrolyte-interphase, current collectors, binders, and

separators, Adv. Energy Mater. 34 (2022) 2108206. https://doi.org/10.1002/adma.202108206.

[6] X. Han, Y. Bai, R. Zhao, Y. Li, F. Wu, C. Wu, Electrolytes for rechargeable aluminum batteries, Prog. Mater. Sci. 128 (2022) 100960. https://doi.org/10.1016/j.pmatsci.2022.100960.

[7] C. Wu, H. Tan, W. Huang, C. Liu, W. Wei, L. Chen, Q. Yan, The strategies to improve the layered-structure cathodes for aqueous multivalent metal-ion batteries, Mater. Today Energy 19 (2021) 100595. https://doi.org/10.1016/j.mtener.2020.100595.

[8] S. Wu, Q. Zhang, J. Ma, D. Sun, Y. Tang, H. Wang, Interfacial design of Al electrode for efficient aluminum-air batteries: issues and advances, Mater. Today Energy 18 (2020) 100499. https://doi.org/10.1016/j.mtener.2020.100499.

[9] R. Bai, J. Yang, G. Li, J. Luo, W. Tang, Rechargeable aqueous aluminum-$FeFe(CN)_6$ battery with artificial interphase through deep eutectic solution, Energy Storage Mater. 41 (2021) 41–50. https://doi.org/10.1016/j.ensm.2021.05.025.

[10] D. Yuan, J. Zhao, W. Manalastas, S. Kumar, M. Srinivasan, Emerging rechargeable aqueous aluminum ion battery: Status, challenges, and outlooks, Nano Mater. Sci. 2 (2020) 248–263. https://doi.org/10.1016/j.nanoms.2019.11.001.

[11] G.R. Pastel, Y. Chen, T.P. Pollard, M.A. Schroeder, M.E. Bowden, A. Zheng, N.T. Hahn, L. Ma, V. Murugesan, J. Ho, M. Garaga, O. Borodin, K. Mueller, S. Greenbaum, K. Xu, A sobering examination of the feasibility of aqueous aluminum batteries, Energy Environ. Sci. 15 (2022) 2460–2469. https://doi.org/10.1039/D2EE00134A.

[12] C. Yan, C. Lv, L. Wang, W. Cui, L. Zhang, K.N. Dinh, H. Tan, C. Wu, T. Wu, Y. Ren, J. Chen, Z. Liu, M. Srinivasan, X. Rui, Q. Yan, G. Yu, Architecting a stable high-energy aqueous Al-ion battery, J. Am. Chem. Soc. 142 (2020) 15295–15304. https://doi.org/10.1021/jacs.0c05054.

[13] E. Faegh, B. Ng, D. Hayman, W.E. Mustain, Practical assessment of the performance of aluminium battery technologies, Nat. Energy 6 (2021) 21–29. https://doi.org/10.1038/s41560-020-00728-y.

[14] W. Pan, Y. Wang, Y. Zhang, H.Y.H. Kwok, M. Wu, X. Zhao, D.Y.C. Leung, A low-cost and dendrite-free rechargeable aluminium-ion battery with superior performance, J. Mater. Chem. A 7 (2019) 17420. https://doi.org/10.1039/C9TA05207K.

[15] W. Wang, B. Jiang, W. Xiong, H. Sun, Z. Lin, L. Hu, J. Tu, J. Hou, H. Zhu, S. Jiao, A new cathode material for super-valent battery based on aluminium ion intercalation and deintercalation, Sci. Rep. 3 (2013) 3383. https://doi.org/10.1038/srep03383.

[16] Y. Cai, S. Kumar, R. Chua, V. Verma, D. Yuan, Z. Kou, H. Ren, H. Arora, M. Srinivasan, Bronze-type vanadium dioxide holey nanobelts as high performing cathode material for aqueous aluminium-ion batteries, J. Mater. Chem. A 8 (2020) 12716. https://doi.org/10.1039/D0TA03986A.

[17] S. Gu, H. Wang, C. Wu, Y. Bai, H. Li, F. Wu, Confirming reversible Al^{3+} storage mechanism through intercalation of Al^{3+} into V_2O_5 nanowires in a rechargeable aluminum battery, Energy Storage Mater. 6 (2017) 9–17. https://doi.org/10.1016/j.ensm.2016.09.001.

[18] H. Wang, X. Bi, Y. Bai, C. Wu, S. Gu, S. Chen, F. Wu, K. Amine, J. Lu, Open-structured $V_2O_5 \cdot nH_2O$ nanoflakes as highly reversible cathode material for monovalent and multivalent intercalation batteries, Adv. Energy Mater. 7 (2017) 1602720. https://doi.org/10.1002/aenm.201602720.

[19] S. Liu, J.J. Hu, N.F. Yan, G.L. Pan, G.R. Li, X.P. Gao, Aluminum storage behavior of anatase TiO_2 nanotube arrays in aqueous solution for aluminum ion batteries, Energy Environ. Sci. 5 (2012) 9743–9746. https://doi.org/10.1039/C2EE22987K.

[20] Y. Liu, S. Sang, Q. Wu, Z. Lu, K. Liu, H. Liu, The electrochemical behavior of Cl^- assisted Al^{3+} insertion into titanium dioxide nanotube arrays in aqueous solution for

aluminum ion batteries, Electrochim. Acta 143 (2014) 340–346. https://doi.org/10.1016/j.electacta.2014.08.016.

[21] T. Koketsu, J. Ma, B.J. Morgan, M. Body, C. Legein, W. Dachraoui, M. Giannini, A. Demortière, M. Salanne, F. Dardoize, H. Groult, O.J. Borkiewicz, K.W. Chapman, P. Strasser, D. Dambournet, Reversible magnesium and aluminium ions insertion in cation-deficient anatase TiO_2, Nat. Mater. 16 (2017) 1142–1150. https://doi.org/10.1038/nmat4976.

[22] A.W. Holland, R. McKerracher, A. Cruden, R.G.A. Wills, TiO_2 nanopowder as a high rate, long cycle life electrode in aqueous aluminium electrolyte, Mater. Today Energy 10 (2018) 208–213. https://doi.org/10.1007/s10800-018-1154-x.

[23] C. Wu, S. Gu, Q. Zhang, Y. Bai, M. Li, Y. Yuan, H. Wang, X. Liu, Y. Yuan, N. Zhu, F. Wu, H. Li, L. Gu, J. Lu, Electrochemically activated spinel manganese oxide for rechargeable aqueous aluminum battery, Nat. Commun. 10 (2019) 73. https://doi.org/10.1038/s41467-018-07980-7.

[24] S. He, J. Wang, X. Zhang, J. Chen, Z. Wang, T. Yang, Z. Liu, Y. Liang, B. Wang, S. Liu, L. Zhang, J. Huang, J. Huang, L.A. O'Dell, H. Yu, A high-energy aqueous aluminum-manganese battery, Adv. Funct. Mater. 29 (2019) 1905228. https://doi.org/10.1002/adfm.201905228.

[25] P. Wang, Z. Chen, Z. Ji, Y. Feng, J. Wang, J. Liu, M. Hu, H. Wang, W. Gan, Y. Huang, A flexible aqueous Al ion rechargeable full battery, Chem. Eng. J. 373 (2019) 580–586. https://doi.org/10.1016/j.cej.2019.05.085.

[26] P. Wang, Z. Chen, H. Wang, Z. Ji, Y. Feng, J. Wang, J. Liu, M. Hu, J. Fei, W. Gan, Y. Huang, A high-performance flexible aqueous Al ion rechargeable battery with long cycle life, Energy Storage Mater. 25 (2020) 426–435. https://doi.org/10.1016/j.ensm.2019.09.038.

[27] S. Liu, G.L. Pan, G.R. Li, X.P. Gao, Copper hexacyanoferrate nanoparticles as cathode material for aqueous Al-ion batteries, J. Mater. Chem. A 3 (2015) 959–962. https://doi.org/10.1039/C4TA04644G.

[28] Z. Li, K. Xiang, W. Xing, W.C. Carter, Y.M. Chiang, Reversible aluminum-ion intercalation in Prussian blue analogs and demonstration of a high-power aluminum-ion asymmetric capacitor, Adv. Energy Mater. 5 (2015) 1401410. https://doi.org/10.1002/aenm.201401410.

[29] A. Holland, R.D. Mckerracher, A. Cruden, R.G.A. Wills, An aluminium battery operating with an aqueous electrolyte, J. Appl. Electrochem. 48 (2018) 243–250. https://doi.org/10.1007/s10800-018-1154-x.

[30] A. Zhou, L. Jiang, J. Yue, Y. Tong, Q. Zhang, Z. Lin, B. Liu C. Wu, L. Suo, Y.S. Hu, H. Li, L. Chen, Water-in-salt electrolyte promotes high-capacity $FeFe(CN)_6$ cathode for aqueous Al-ion battery, ACS Appl. Mater. Interfaces 11 (2019) 41356–41362. https://doi.org/10.1021/acsami.9b14149.

[31] Y. Gao, H. Yang, X. Wang, Y. Bai, N. Zhu, S. Guo, L. Suo, H. Li, H. Xu, C. Wu, The compensation effect mechanism of Fe-Ni mixed Prussian blue analogues in aqueous rechargeable aluminum-ion batteries, ChemSusChem 13 (2020) 732–740. https://doi.org/10.1002/cssc.201903067.

[32] Y. Ru, S. Zheng, H. Xue, H. Pang, Potassium cobalt hexacyanoferrate nanocubic assemblies for high-performance aqueous aluminum ion batteries, Chem. Eng. J. 382 (2020) 122853. https://doi.org/10.1016/j.cej.2019.122853.

[33] D. Wang, H. Lv, T. Hussain, Q. Yang, G. Liang, Y. Zhao, L. Ma, Q. Li, H. Li, B. Dong, T. Kaewmaraya, C. Zhi, A manganese hexacyanoferrate framework with enlarged ion tunnels and two-species redox reaction for aqueous Al-ion batteries, Nano Energy 84 (2021) 105945. https://doi.org/10.1016/j.nanoen.2021.105945.

[34] T. Xiong, B. He, T. Zhou, Z. Wang, Z. Wang, J. Xin, H. Zhang, X. Zhou, Y. Liu, L. Wei, Stretchable fiber-shaped aqueous aluminum ion batteries. EcoMat (2022) e12218. https://doi.org/10.1002/eom2.12218.

[35] F. Scholz, A. Dostal, The formal potentials of solid metal hexacyanometalates, Angew. Chem. Int. Ed. Engl. 34 (1996) 2685–2687. https://doi.org/10.1002/anie.199526851.

[36] R.Y. Wang, B. Shyam, K.H. Stone, J.N. Weker, M. Pasta, H.W. Lee, M.F. Toney, Y. Cui, Reversible multivalent (monovalent, divalent, trivalent) ion insertion in open framework materials, Adv. Energy Mater. 5 (2015) 1401869. https://doi.org/10.1002/aenm.201401869.

[37] J. Wu, J. Song, K. Dai, Z. Zhuo, L.A. Wray, G. Liu, Z. Shen, R. Zeng, Y. Lu, W. Yang, Modification of transition-metal redox by interstitial water in hexacyanometalate electrodes for sodium-ion batteries. J. Am. Chem. Soc. 139 (2017) 18358–18364. https://doi.org/10.1021/jacs.7b10460.

[38] F. Herren, P. Fischer, A. Ludi, W. Hälg, Neutron diffraction study of Prussian blue, $Fe_4[Fe(CN)_6]_3 \cdot xH_2O$. Location of water molecules and long-range magnetic order, Inorg. Chem. 19 (1980) 956–959. https://doi.org/10.1021/ic50206a032.

[39] S.S. Kaye, J.R. Long, Hydrogen storage in the dehydrated Prussian blue analogues $M_3[Co(CN)_6]_2$ (M=Mn, Fe, Co, Ni, Cu, Zn), J. Am. Chem. Soc. 127 (2005) 6506–6507. https://doi.org/10.1021/ja051168t.

[40] C. Gao, Y. Liu, B. Cheng, J. Yun, E. Feng, Y. Kim, M. Kim, A. Choi, H.W. Lee, S.W. Lee, Efficient low-grade heat harvesting enabled by tuning the hydration entropy in an electrochemical system, Adv. Mater. 33 (2021) 2004717. https://doi.org/10.1002/adma.202004717.

[41] S.W. Lee, Y. Yang, H.W. Lee, H. Ghasemi, D. Kraemer, G. Chen, Y. Cui, An electrochemical system for efficiently harvesting low-grade heat energy, Nat. Commun. 5 (2014) 3942. https://doi.org/10.1038/ncomms4942.

[42] K. Hurlbutt, S. Wheeler, I. Capone, M. Pasta, Prussian blue analogs as battery materials, Joule 2 (2018) 1950–1960. https://doi.org/10.1016/j.joule.2018.07.017.

[43] E. Levi, Y. Gofer, D. Aurbach, On the way to rechargeable Mg batteries: the challenge of new cathode materials, Chem. Mater. 22 (2010) 860. https://doi.org/10.1021/cm9016497.

[44] X. Wu, N. Qin, F. Wang, Z. Li, J. Qin, G. Huang, D. Wang, P. Liu, Q. Yao, Z. Liu, J. Deng, Reversible aluminum ion storage mechanism in Ti-deficient rutile titanium dioxide anode for aqueous aluminum-ion batteries, Energy Storage Mater. 37 (2021) 619–627. https://doi.org/10.1016/j.ensm.2021.02.040.

[45] X. Wu, J.J. Hong, W. Shin, L. Ma, T. Liu, X. Bi, Y. Yuan, Y. Qi, T.W. Surta, W. Huang, J. Neuefeind, T. Wu, P.A. Greaney, J. Lu, X. J, Diffusion-free Grotthuss topochemistry for high-rate and long-life proton batteries, Nat. Energy 4 (2019) 123–130. https://doi.org/10.1038/s41560-018-0309-7.

Brief bio for authors

Xiaoya Li is currently a Research Fellow in School of Electrical and Electronic Engineering, Nanyang Technological University, Singapore. She received her B.E. and Ph.D. degree from Tianjin University, China, in 2014 and 2020. She worked as a postdoc in University of Science and Technology of China prior to NTU. Her research interests are high-performance and cost-effective energy technologies and component design, energy harvesting, electrochemical energy storage, and vehicle thermal management.

Angyin Wu received his BEng (2017) from Huazhong University of Science and Technology (HUST; China) and his MEng (2018) from The University of Queensland (UQ; Australia). He is currently a Ph.D. candidate in the School of Electrical and Electronic Engineering in Nanyang Technology University (EEE, NTU) under the supervision of Prof. Seok Woo Lee. His research is focused on electrode materials of aqueous batteries and thermal energy harvesting using thermally regenerative electrochemical cycle.

Caitian Gao is currently an associate professor in the School of Physics and Electronics at Hunan University. She received her Ph.D. in Condensed Matter Physics from Lanzhou University in 2015. Her research interests include energy harvesting, electrochemical energy storage and low temperature thermodynamic behavior in alkaline metal batteries.

Seok Woo Lee is an assistant professor in the School of Electrical and Electronic Engineering, Nanyang Technological University. He was a postdoctoral scholar and a research associate in Stanford University. He received B.S. and Ph.D. from POSTECH and KAIST, respectively. He has worked on nanomaterials for electrochemical energy storage and conversion. In addition, he has utilized the microfabrication to develop various functional energy storage and harvesting systems.